Acta Mechanica 175, 197–215 (2005)
DOI 10.1007/s00707-004-0117-y

Acta Mechanica
Printed in Austria

Propulsive performance of a fish-like travelling wavy wall

X.-Y. Lu and **X.-Z. Yin,** Hefei, China

Received October 21, 2003; revised March 8, 2004
Published online: February 24, 2005

Summary. A numerical simulation is performed to investigate the viscous flow over a smooth wavy wall undergoing transverse motion in the form of a streamwise travelling wave, which is similar to the backbone undulation of swimming fish. The objective of this study is to elucidate hydrodynamic features of the flow structure over the travelling wavy wall and to get physical insights to the understanding of fish-like swimming mechanisms in terms of drag reduction and optimal propulsive efficiency. The effect of phase speed, amplitude and Reynolds number on the flow structure over the wavy wall, the drag force acting on the wall, and the power consumption required for the propulsive motion of the wall is investigated. The phase speed and the amplitude, which are two important parameters in this problem, predicted based on the optimal propulsive efficiency agree well with the available data obtained for the wave-like swimming motion of live fish in nature.

1 Introduction

A biofluiddynamics of fish locomotion was founded by Lighthill with a theory for evaluating reactive forces between an undulating fish body and the water surrounding it [1], [2]. Further development of the subject was carried out and comprehensive reviews of relevant work can be found in [3]–[5]. To better explore the swimming ability of these live, the interactions between the swimming body and fluid need to be studied to understand the physical mechanisms. Both the wave-like swimming and flapping motions of the body are essential to the propulsion of fish. Previously researchers have shown the ability of the caudal fin of a fish to produce a jet-like wake similar to that of a flapping foil [6]–[10]. While the undulating body motions produce the locomotion, it is not yet clear exactly how the body undulating motion effects the flow very near a fish or a travelling wave wall.

As is well known, fish use predominantly oscillatory movements [11]. Gray noted that fish swimming movement is mainly described as a combination of two wave-like phenomena [12]. One is cyclic change of the curved shape of the body showing a lateral wave of curvature running in the caudal direction, and the other is every single point of the body performing, in consequence of the wave of lateral curvature on the body, a sinusoidal track in a horizontal plane. Thus, a travelling wavy wall problem is of interest parallel to the swimming fish, since the backbone motion of fish species is essentially that of the travelling wave. Actually, the model is appropriate for anguilliform, subcarangiform, and carangiform swimmers [13]–[15].

Fish swimming can be very instructive in disclosing mechanisms of unsteady flow control, which was raised first in the relation to swimming of live fish. Gray [16] observed that an

actively swimming dolphin only consumes one seventh of the energy needed to tow a rigid body at the same speed, and suggested that substantial drag reduction must occur in the live dolphin. Then, much work has been performed to explore this problem. Important contributions by Lighthill [2] and Wu [17], [18] have shed light on the inviscid hydrodynamics of fish-like propulsion. Cheng et al. [19] analyzed the swimming propulsion mechanism of a three-dimensional plate moving in an inviscid fluid. Based on experimental investigation, Aleyev [20] and Harper and Blake [21] reported the outstanding performance by fish and led to interest in fish-like vehicles capable of emulating the high performance of fish propulsion and maneuvering. Barrett et al. [22] found that the power required to propel a swimming body may be smaller than that needed to tow a straight-rigid body.

It has been proposed that the travelling wave motion contributes to reducing drag force and increasing propulsive efficiency by restraining separation [23], [24]. Viscous flow past a travelling wavy wall, in which the wall wavy displacements propagate in the streamwise direction, differs from the flow near a fixed wavy wall. The flow over the wavy wall is strongly affected by surface normal pressure gradient and centrifugal force due to alternating convex and concave curvatures. The effects of a surface normal pressure gradient are evident as the flow over a rotationally oscillating cylinder, in which flow separation can be reduced as observed experimentally by Tokumaru and Dimotakis [25], and numerically by Lu and Sato [26] and Lu [27]. Experiments were undertaken to investigate viscous flow past a travelling wavy wall. Taneda and Tomonari [28] observed that the boundary layer separates at the back of the wave crest for the travelling wave phase speed being smaller than the external flow velocity, but the boundary layer does not separate for the wave phase speed being larger than the external flow velocity. Kendall [29] investigated the effect of a travelling wavy wall on flow behavior. Meanwhile, numerical simulations [30], [31] have been performed for viscous flow over a fixed wavy surface and confirmed the previous experimental measurements.

To understand fish swimming propulsion, it is needed to study two typical problems including the nature of the force resisting the motion and the mechanisms that lead to the thrust force [24]. In this study, computational fluid dynamics is applied to investigate viscous flow over a travelling wavy wall. We recognize the limitation of this model for modeling fish swimming, in which fish are of finite length, shed vortices unsteadily in their wake, and experience force on both sides of its body. However, we still feel that the results will be of fundamental use in exploring the hydrodynamic feature of the flow near the travelling wavy wall and in getting into physical understanding of fish-like swimming mechanisms.

This paper is organized as follows. The physical problem and mathematical formulations are described in Sect. 2. The numerical method and its validation are briefly given in Sect. 3. In Sect. 4, the flow structure, the drag force and the power consumption are analyzed and discussed.

2 Physical problem and mathematical formulation

As shown schematically in Fig. 1, viscous flow over a moving wall undergoing a travelling wave motion is considered. Two-dimensional incompressible Navier-Stokes equations are employed as governing equations. To nondimensionalize the equations, the wavelength λ is used as the length scale, and the mean velocity of the external flow U as the velocity scale. Then, the nondimensional equations are given by

$$\frac{\partial u_i}{\partial x_i} = 0, \tag{1}$$

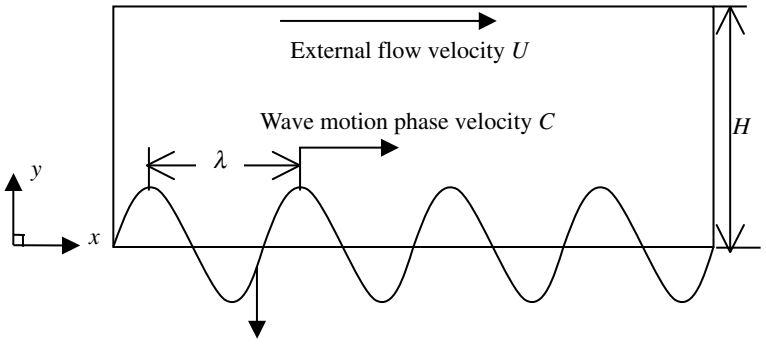

Fig. 1. Sketch of the physical problem

$$\frac{\partial u_i}{\partial t} + \frac{\partial}{\partial x_j}(u_i u_j) = -\frac{\partial p}{\partial x_i} + \frac{1}{\mathrm{Re}}\nabla^2 u_i, \tag{2}$$

where Re is the Reynolds number defined as $\mathrm{Re} = U\lambda/\nu$ with ν the kinematic viscosity. The pressure p is normalized by ρU^2 where ρ is the fluid density.

The wall is taking a vertical oscillation in the form of a wave travelling in the streamwise direction, and the position of the wall is described by

$$y_w = A\sin k(x - Ct), \tag{3}$$

where A and C are the amplitude and the phase speed of the travelling wave, $k = 2\pi/\lambda$ is the wave number, and the subscript w denotes the quantity on the wall. Here, the steepness of the travelling wave is represented as $\sigma = 2\pi A/\lambda$. The moving wall possesses an up-down oscillation with velocity components shown as

$$u_w = 0, \quad v_w = -kCA\cos k(x - Ct), \tag{4}$$

where u and v represent the velocity component in the x- and y-direction, respectively.

In this study, the frame is chosen as moving with the phase velocity of the travelling wave. This approach can simplify the numerical scheme by eliminating the time-derivative terms in grid generation, at the expense of modifying the velocity boundary conditions according to the phase speed of the wave. Then, the wavy surface becomes stationary and fluid elements on the wall have a nonzero horizontal velocity $-C$. The corresponding boundary conditions at the upper boundary (i.e., at $y = H$) are $u = 1 - C$, $v = 0$, and $\partial p/\partial y = 0$. Periodic boundary conditions are employed in the streamwise direction. The height of the upper boundary is chosen as $H/\lambda = 2$. It will be confirmed that, in the following section, the domain size is large enough to have little influence on the calculated results.

3 Numerical method and validation

A frictional step method is used to solve Eqs. (1) and (2). The time advancement is approximated with the Adams-Bashforth method for the convective terms and the Crank-Nicholson for the viscous terms. The convective terms are discretized using a variation of QUICK [32]. The pressure is obtained by solving the pressure Poisson equation with a multigrid method [33]. Detailed discretizations were described by Zang et al. [32].

The computational domain in Fig. 1 is chosen as $0 \leq x/\lambda \leq 1$ in the x-direction and the height of the upper boundary $H/\lambda = 2$ in the y-direction, with the grid number 256×256. A time step is determined as 0.0002 based on the computation stability condition. The grid is uniform along the x-direction. To increase the grid resolution near the wavy wall boundary, the mesh is stretched in the y-direction following the transformation used by Lu [34], [35].

Extensive convergence checks with different grid sizes, time steps and computational domains have been carried out. As a typical case, Fig. 2 shows the distribution of the streamwise component of friction force acting on the wavy wall at $\sigma = 0.25$, $C = 1.0$ and $\mathrm{Re} = 2000$. Four cases are considered, and these results agree well with each other. It means that the calculated result converges as the grid, time step and computation domain are varied independently. The present computational code was also verified by our previous work [34]–[36]. Thus, it can be confirmed that our calculation is reliable for the prediction of the behaviors of flow and force for the flow over a travelling wavy wall.

4 Results and discussion

The computational parameters are chosen as follows: the phase speed C ranges from –1.0 to 2.0 with 0.2 interval, the wave steepness σ is 0.125, 0.25, and 0.5, and the Reynolds number Re is 400, 2000 and 5000, respectively.

4.1 Flow structures

Flow structures are based on the streamline patterns and the vorticity contours. The streamline topology pattern provides an overall picture of the flow near the wavy wall, and the vorticity contours clearly depict the character of the shear layer over the travelling wall boundary. Some typical results for $\mathrm{Re} = 2000$ and $\sigma = 0.25$ with different phase speeds are analyzed.

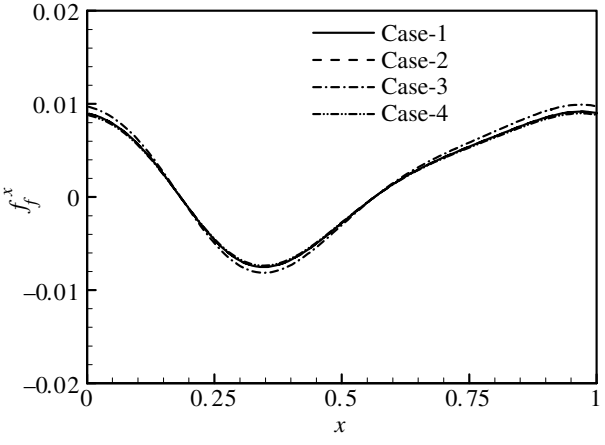

Fig. 2. Computation validation based on the distribution of the streamwise component of friction force acting on the wavy wall at $\sigma = 0.25$, $C = 1.0$ and $\mathrm{Re} = 2000$. *Case 1*: grid number $N = 256 \times 256$, time step $\Delta t = 0.0002$, computational domain $0 \leq x/\lambda \leq 1$ and $H/\lambda = 2$; *Case 2*: phase-averaged value by use of 4-wavelength data with $N = (4 \times 256) \times 256$, $\Delta t = 0.0002$, $0 \leq x/\lambda \leq 4$ and $H/\lambda = 2$; *Case 3*: $N = 512 \times 512$, $\Delta t = 0.0001$, $0 \leq x/\lambda \leq 1$ and $H/\lambda = 2$; *Case 4*: $N = 256 \times 512$, $\Delta t = 0.0002$, $0 \leq x/\lambda \leq 1$ and $H/\lambda = 4$

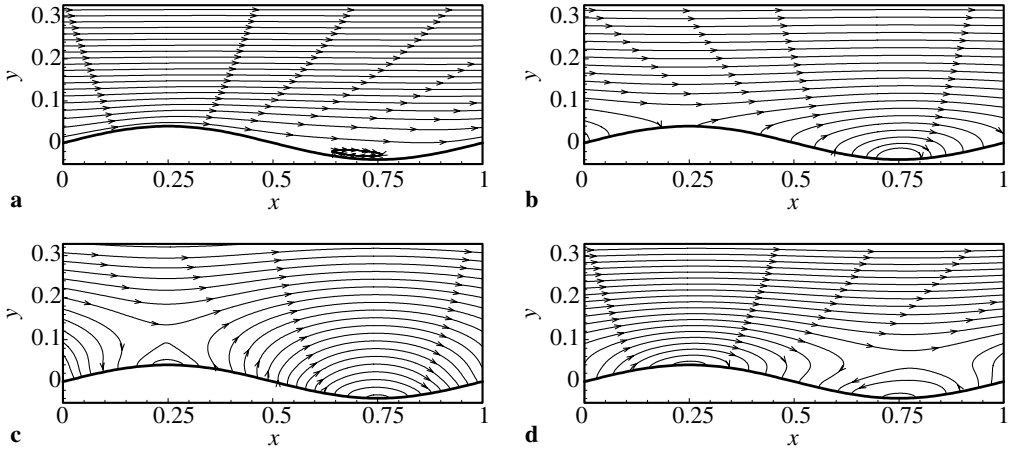

Fig. 3. Streamline pattern in the non-moving frame at $\mathrm{Re} = 2000$ and $\sigma = 0.25$: **a** $C = 0$; **b** $C = 0.4$; **c** $C = 1.2$; **d** $C = -0.4$

Figure 3 shows the streamline patterns with different phase speeds in the non-moving frame. When flow passes the crest if the wave is sufficiently steep for a stationary wall (i.e., $C = 0$), a separation bubble is formed near the trough (Fig. 3a). When the wavy wall is travelling in the x-direction, the wall boundary is no longer a streamline and there are streamlines that emanate from the surface and end on the surface. For $C > 0$, the right side of the crest rises and the left side descends. The vertical flow induced by the wall waving motion increases with the increase of C. The streamlines above the trough become convex for $C = 0.4$ and 1.2 in Figs. 3b and 3c, while they are concave for $C = 0$ in Fig. 3a. The streamlines at $C = -0.4$ are shown in Fig. 3d, and a flow reversal region with concave streamlines appears above the trough.

In the moving frame, the horizontal velocity component equals $-C$ at the wall and $1 - C$ far away. Therefore, when $0 < C < 1$, the horizontal velocity must change its sign along the vertical direction from the wall to the external region. The streamlines for $C = 0.4$ and 0.8 exhibit a trapped vortex located over the trough in Fig. 4a and b. Note that the pattern for $C = 0$ is identical to Fig. 3a. If C exceeds the external flow velocity (i.e., $C > 1$), both $-C$ and $1 - C$ are negative. The streamline pattern at $C = 1.2$ is shown in Fig. 4c; all the streamlines point in the negative x-direction and there is no trapped vortex. As shown in Fig. 4d for the streamlines at $C = -0.4$, no trapped vortex exists for $C < 0$, because both the wall speed $-C$ and the external flow velocity $1 - C$ are moving in the positive x-direction.

Figure 5 shows the vorticity contours in the near wall region. The vorticity contours exhibit the free shear layer behind the crest for $C = 0$ in Fig. 5a, and are rolling-up over the trough for $C = 0.8$ in Fig. 5b, where a trapped vortex occurs. With the increase of C, as shown in Fig. 5c, the separation is suppressed for $C = 1.2$. The shear layers are generated along the wall over the crest with positive vorticity and over the trough with negative vorticity. For $C < 0$, the vorticity contours at $C = -0.4$ are shown in Fig. 5d. It can be noted that the shear layers are formed over the crest with negative vorticity and over the trough with positive vorticity.

4.2 Drag force and power consumption

The drag force acting on the wavy surface and the power needed for it to be propelled are directly relevant to the study of fish locomotion. The total drag force on the wavy wall consists

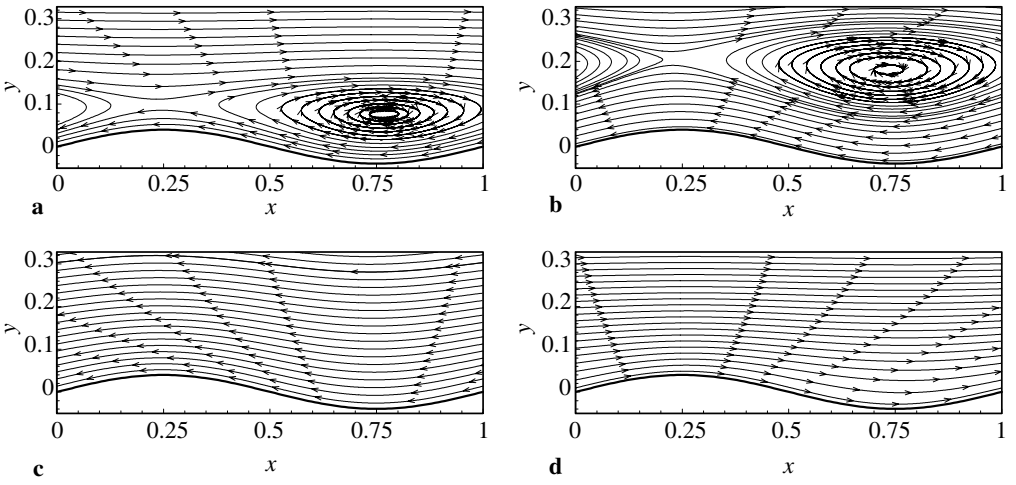

Fig. 4. Streamline pattern in the moving frame at $\mathrm{Re} = 2000$ and $\sigma = 0.25$: **a** $C = 0.4$; **b** $C = 0.8$; **c** $C = 1.2$; **d** $C = -0.4$

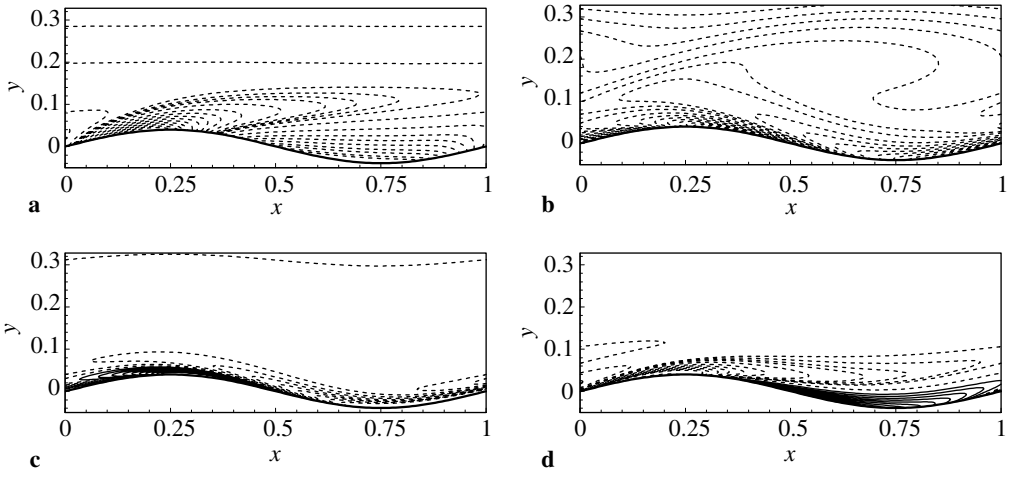

Fig. 5. Vorticity contours at $\mathrm{Re} = 2000$ and $\sigma = 0.25$: **a** $C = 0$; **b** $C = 0.8$; **c** $C = 1.2$; **d** $C = -0.4$. Solid lines represent positive values and dashed lines negative values with an increment 1.0

of a friction drag and a form drag due to pressure distribution. In Fig. 1, for an element of the wall surface $ds = [1 + (dy_w/dx)^2]^{1/2}$, its tangential direction is $\vec{t} = (1,\ dy_w/dx)/ds$ and the wall-normal direction is $\vec{n} = (-dy_w/dx,\ 1)/ds$. Then, the friction force and the pressure force per unit length along the wall can be accurately expressed as [24], [37]

$$f_f^x = \frac{1}{\mathrm{Re}}\Big[-2\frac{\partial u}{\partial x}\frac{dy_w}{dx} + \Big(\frac{\partial u}{\partial y} + \frac{\partial v}{\partial x}\Big)\Big] \quad \text{on } y = y_w, \tag{5.1}$$

$$f_p^x = p\frac{dy_w}{dx} \text{ on } y = y_w. \tag{5.2}$$

By performing integration of f_f^x and f_p^x over the wavy surface, the friction force F_f, the pressure force F_p, and the total drag force $F_d = F_f + F_p$ can be obtained.

Based on the definition [24], the total power (P_T) required for the propulsive motion of the wall consists of two parts. One is the swimming power $P_s = \int p(dy_w/dt)dx$ required to produce the vertical oscillation of travelling wave motion, and the other is the power, $P_d = UF_d$, needed to overcome the drag force. Thus, the total power $P_T = P_s + P_d$ is calculated.

Figure 6 shows the variations of drag force and power versus C at $\mathrm{Re} = 2000$ and $\sigma = 0.25$. In Fig. 6a, as C increases, the friction force F_f increases, the pressure force F_p decreases monotonically, and the total drag force F_d decreases. When $C > 1.6$ approximately, F_d becomes negative and acts as thrust force.

The distributions of P_T, P_s and P_d versus C are shown in Fig. 6b. As C increases, P_s first decreases, then reaches a minimum for C between 0 and 1, finally increases. For $C < 0$, the sign of dy_w/dt is reversed but the pressure distribution difference persists, so that P_s is still positive. At $C = 0$, $P_s = 0$ because $dy_w/dt = 0$. When C (for $C > 0$) increases, flow separation is suppressed and the pressure gradient is mainly influenced by the wavy wall motion. The negative value of P_s means that the wall motion can be actuated by the flow and no power input is needed for $0.2 < C < 0.8$, approximately. P_s becomes positive for $C \geq 1$. As C increases further, flow separation eventually occurs upstream of the crest and P_s increases rapidly. The power to overcome the drag force, P_d, decreases monotonically with the increase of C, because of the similar decrease of F_d, as shown in Fig. 6a. When P_d is negative, it means that the wavy

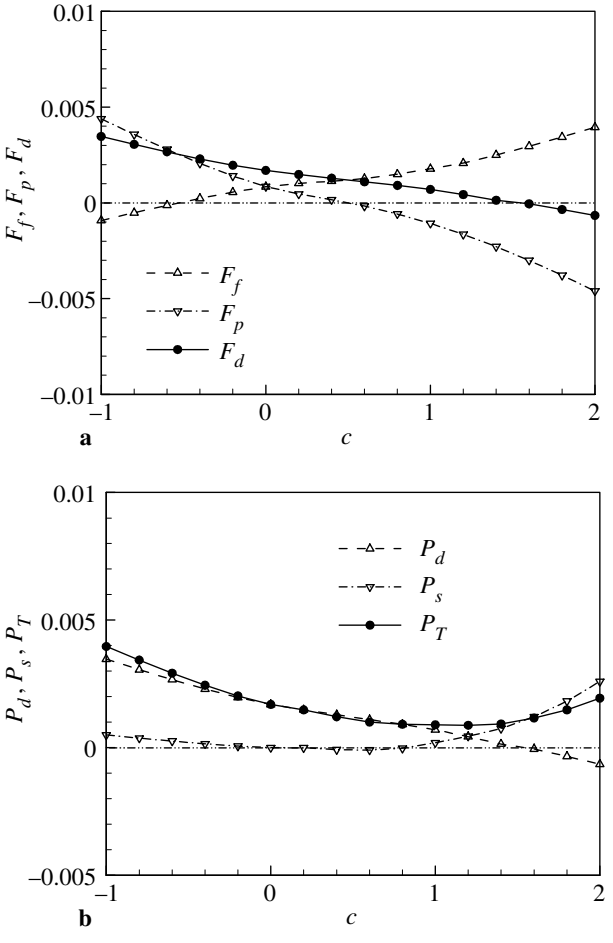

Fig. 6. Variations of the drag force and the power versus C at $\mathrm{Re} = 2000$ and $\sigma = 0.25$: **a** drag force; **b** power

surface is propelled by the thrust; however, the thrust is at the expense of the swimming power P_s required to produce the wavy wall motion. Both P_d and P_s present the competing mechanisms. As shown in Fig. 6b, the distribution of the total power P_T versus C is concave upwards with a minimum around $C = 1.2$, which is consistent with the value used for travelling wave-like swimming motion of live fish in nature [38], [39].

To demonstrate the propulsive efficiency, the total power ratio of the optimal propulsion with the minimal power ($P_T|_{C\ \mathrm{opt}}$) and the stationary wavy wall with the power $P_T|_{C=0}$ is defined as $\eta = (P_T|_{C\ \mathrm{opt}})/(P_T|_{C=0})$. As listed in Table 1, the power ratio η is 52% approximately for the phase speed with the optimal propulsion corresponding to $C = 1.2$ at $\mathrm{Re} = 2000$ and $\sigma = 0.25$, so that there is a significant gain in net efficiency as a result of the travelling wave motion.

To explain the effects of C on the drag force and the power, Fig. 7 shows the distributions of f_f^x and f_p^x along the wavy surface. The distributions exhibit substantial variation for f_f^x and f_p^x. The friction force appears with negative value for $C \leq -0.6$, approximately. Typically, at $C = -0.8$, it is noted that the negative friction force is mainly distributed over the trough region. At $C = 0$, f_f^x increases somewhat over the region of $0 < x < 0.25$ and decreases thereafter. As C increases, e.g., $C = 0.8$ and 1.2, f_f^x is mainly distributed in the regions of the trough and the upstream of the crest. The form drag due to the pressure distribution is shown in Fig. 7b. At $C = 0$, the pressure force shows mainly a small positive value, and consequently the net form drag is formed. The contributions on both the sides of the crests (and trough) are obvious and almost cancel. The net form drag is positive at $C = -0.8$ and -0.4, and negative at $C = 0.8$ and 1.2.

4.3 Effect of the steepness on the flow structure, drag force and power consumption

Figure 8 shows the streamline patterns for $\sigma = 0.125$ and 0.5 with $\mathrm{Re} = 2000$ in the non-moving frame. The corresponding streamline pattern for $\sigma = 0.25$ is exhibited in Fig. 3. When $C > 0$, e.g., $C = 0.4$ and 1.2 in Fig. 8, as σ increases, the vertical flow induced by the wall waving motion increases and the convex shape of the streamlines becomes more obvious. When $C < 0$, e.g., $C = -0.4$ in Fig. 8, a flow reversal region appears above the trough, and the streamlines over the reversal region are concave. The concave shape of the streamlines becomes more obvious with the increase of σ.

The streamline patterns for $\sigma = 0.125$ and 0.5 with $\mathrm{Re} = 2000$ in the moving frame are shown in Fig. 9. For stationary wall (i.e., $C = 0$), if the wave is sufficiently steep, a separation bubble is formed near the trough. The separation bubble is formed at $\sigma = 0.25$ (Fig. 3a) and 0.5, however, no separation bubble occurs at $\sigma = 0.125$. When $0 < C < 1$, the streamlines, e.g., at $C = 0.4$ in Fig. 9, exhibit a trapped vortex located over the trough. By comparing with Fig. 4a for $\sigma = 0.25$, the scale of the trapped vortex increases as σ increases. When $C > 1$, both $-C$ and $1 - C$ are negative. All the streamlines point in the opposite x-direction for $C = 1.2$,

Table 1. Total power ratio between $C = C_{\mathrm{opt}}$ and $C = 0$

Re	σ	P_T at $C = 0$	P_T at $C = C_{\mathrm{opt}}$	$\eta = P_T\|_{C\mathrm{opt}}/P_T\|_{C=0}$
400	0.25	3.561×10^{-3}	2.433×10^{-3}	68 %
2000	0.25	1.691×10^{-3}	8.774×10^{-4}	52 %
5000	0.25	1.263×10^{-3}	6.045×10^{-4}	48 %
2000	0.125	1.351×10^{-3}	1.155×10^{-3}	85 %
2000	0.50	1.788×10^{-3}	3.521×10^{-4}	20 %

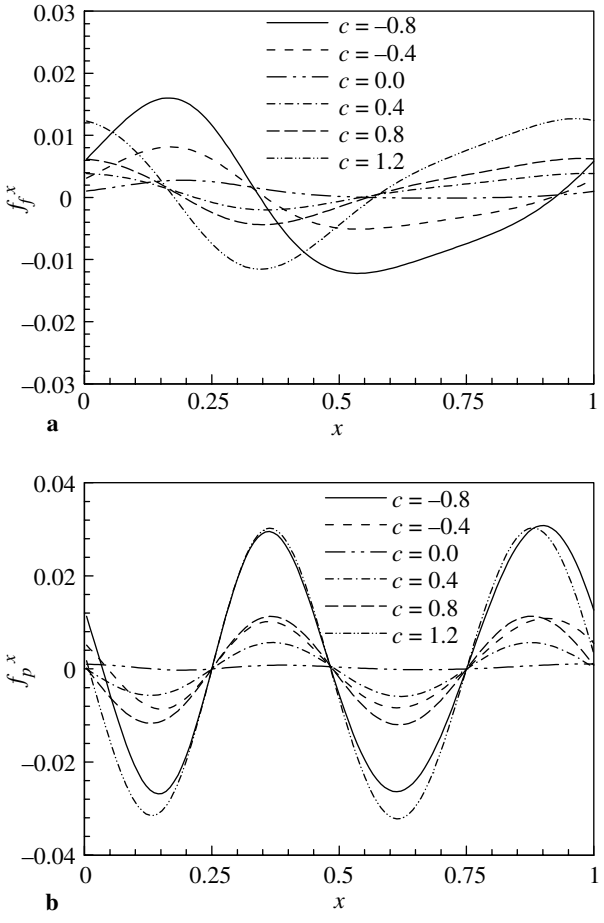

Fig. 7. Distributions of the streamwise component of the friction and the pressure force at $\mathrm{Re} = 2000$ and $\sigma = 0.25$: **a** friction force; **b** pressure force

and there is no trapped vortex. When $C < 0$, e.g., $C = -0.4$ in Fig. 9, no vortex does exist, too, as both the wall speed $-C$ and the external flow velocity $1 - C$ are moving in the x-direction.

Figure 10 shows the profiles of the friction force F_f, the pressure force F_p and the total drag force $F_d = F_f + F_p$. As C increases for different σ, F_f increases, but F_p decreases monotonically. In Fig. 10a, it is found that F_f at $C = -1.0$ is positive for $\sigma = 0.125$ and negative for $\sigma = 0.25$ and 0.5. Meanwhile, F_f increases quickly with the increase of σ. Thus, F_f changes from negative to positive value around $C = -0.4$ for $\sigma = 0.25$ and around $C = 0$ for $\sigma = 0.5$. The profiles of F_f intersect at $C = 0.4$ approximately. At $C = 2.0$, F_f increases with the increase of σ.

To analyze the form drag due to the pressure distribution on the wall, as shown in Fig. 10b, the profiles of F_p intersect and change from positive to negative value at $C = 0.4$, approximately. The negative value of F_p means that the pressure force contributes a thrust force for the travelling wavy wall. At $C = 2.0$, F_p has lower negative value for higher σ; it means that F_p can provider higher propulsive force for larger amplitude of the travelling wavy wall. The behavior is qualitatively consistent with our visualization of fish swimming [40]. As shown in Fig. 10c for the total drag force, F_d is nearly a positive constant at $\sigma = 0.125$; however, when σ increases, F_d becomes negative (or thrust force) for $C \geq 1.6$ approximately at $\sigma = 0.25$ and for $C \geq 1$ at $\sigma = 0.5$. Note that a certain amplitude of the undulating wave motion is needed to generate an efficient locomotion.

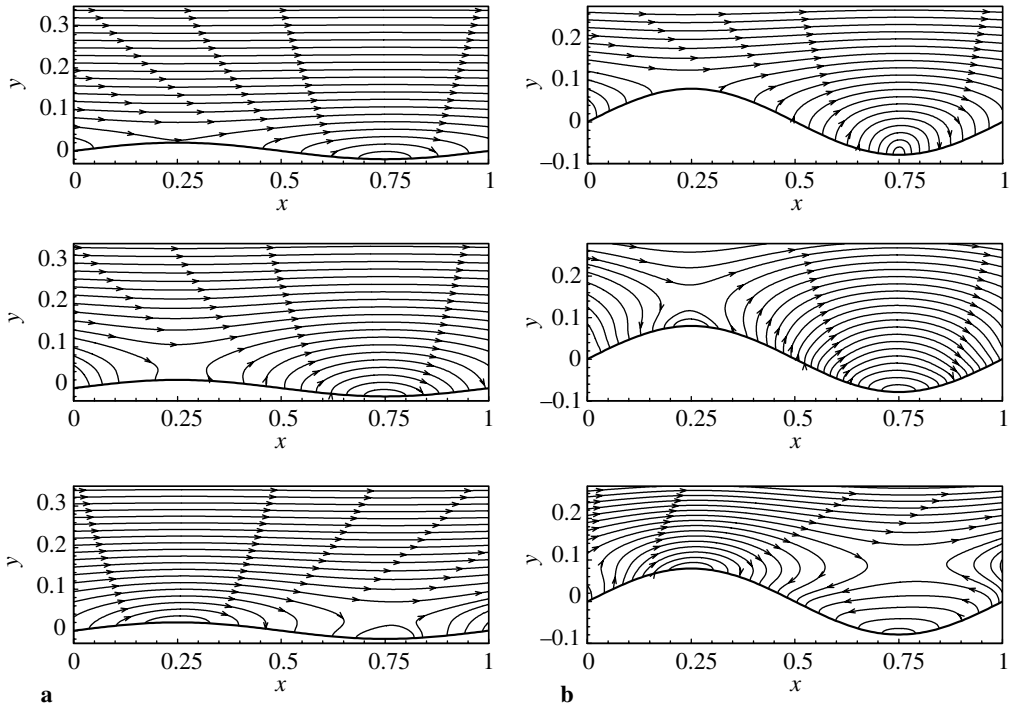

Fig. 8. Streamline pattern in the non-moving frame for different σ at $\mathrm{Re} = 2000$: **a** left column with $\sigma = 0.125$, $C = 0.4$, 1.2, and -0.4 from top to bottom; **b** right column with $\sigma = 0.5$, $C = 0.4$, 1.2, and -0.4 from top to bottom

Figure 11 shows the distributions of P_T and P_s. As C increases, P_s first decreases smoothly, reaches a minimum for C between 0 and 1.0, and then increases quickly, in particular for $\sigma = 0.5$. When $C < 0$, the sign of dy_w/dt is reversed but the pressure distribution difference persists, so that P_s is still positive. P_s is negative for $0.2 \leq C \leq 0.8$ approximately and becomes positive for $C \geq 1$. As C increases further, flow separation eventually occurs upstream of the crest and P_s increases rapidly, in particular for $\sigma = 0.5$. The profiles of the power to overcome the drag force, i.e., P_d, are shown in Fig. 10c for different σ. P_d decreases monotonically with the increase of C. Similar to the behavior of the total drag F_d, P_d is nearly a positive constant at $\sigma = 0.125$, and P_d becomes negative for $C \geq 1.6$ approximately at $\sigma = 0.25$ and for $C \geq 1$ at $\sigma = 0.5$. Even though P_d is negative for large C, the thrust is at the expense of the swimming power P_s required to produce the wavy wall motion, and needs more cost of P_s at higher σ.

The distributions of the total power P_T versus C are shown in Fig. 11b and are concave upwards with a minimum around $C = 1.2$, which corresponds to the optimal phase speed approximately. As listed in Table 1, the total power ratio η is 85% approximately for $\sigma = 0.125$, and only 20% for $\sigma = 0.5$.

To examine the effect of the steepness σ on the total power ratio η, as a typical case, Fig. 12 shows the variation of η versus σ at $C = 1.2$ and $\mathrm{Re} = 2000$. Note that a significant efficiency, corresponding to lower η, for the travelling wave motion exists in the range of $0.4 < \sigma < 0.7$, approximately. Thus, it can reasonably be proposed that there is a possibly optimal steepness (or amplitude) to generate a high propulsive efficiency for the travelling wavy wall.

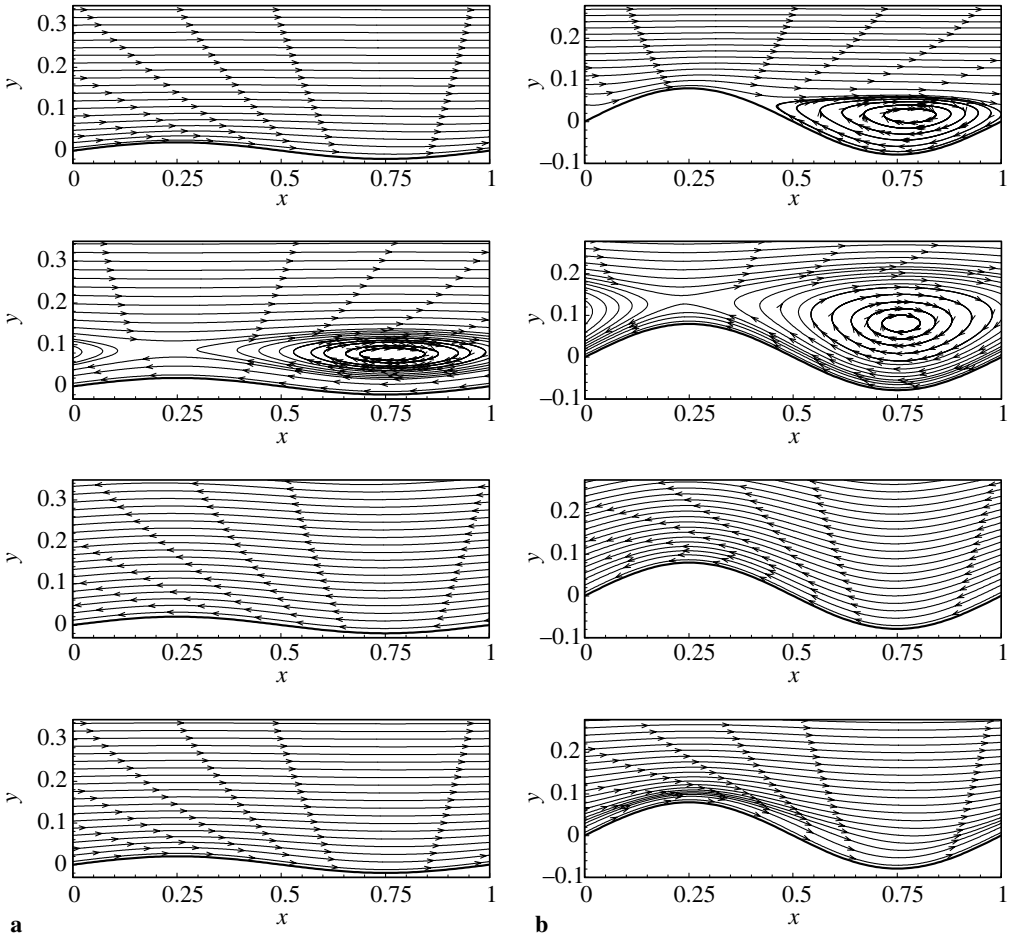

Fig. 9. Streamline pattern in the moving frame for different σ at $\mathrm{Re} = 2000$: **a** left column with $\sigma = 0.125$, $C = 0$, 0.4, 1.2, and -0.4 from top to bottom; **b** right column with $\sigma = 0.5$, $C = 0$, 0.4, 1.2, and -0.4 from top to bottom

4.4 Effect of the Reynolds number on the flow structure, drag force and power consumption

The effect of the Reynolds number on the flow structure, the drag force and the power consumption is analyzed for $\mathrm{Re} = 400$, 2000 and 5000 with $\sigma = 0.25$. It is needed to indicate that the present calculations are two-dimensional for $\mathrm{Re} = 5000$ based on the observations [28], [29] that the near wall structure was essentially two-dimensional due to the forced wavy wall motion. Meanwhile, it is noted that the flow is still steady for $\mathrm{Re} = 5000$ and $\sigma = 0.25$ at different phase speeds by examining our calculated results.

Figure 13 shows the streamline pattern for $\mathrm{Re} = 400$ and 5000 with $\sigma = 0.25$ in the non-moving frame. The corresponding streamline pattern at $\mathrm{Re} = 2000$ is exhibited in Fig. 3. For $C > 0$, e.g., $C = 0.4$ and 1.2 in Fig. 13, because the vertical flow is induced by the wall waving motion, the convex shape of the streamlines becomes more obvious when Re decreases. It can be explained by the fact that viscous diffusive effect induces some differences in the streamline patterns. For $C < 0$, e.g., $C = -0.4$ in Fig. 13, a flow reversal region with concave streamlines above the trough occurs, and the concave shape of the streamlines becomes more pronounced as Re decreases.

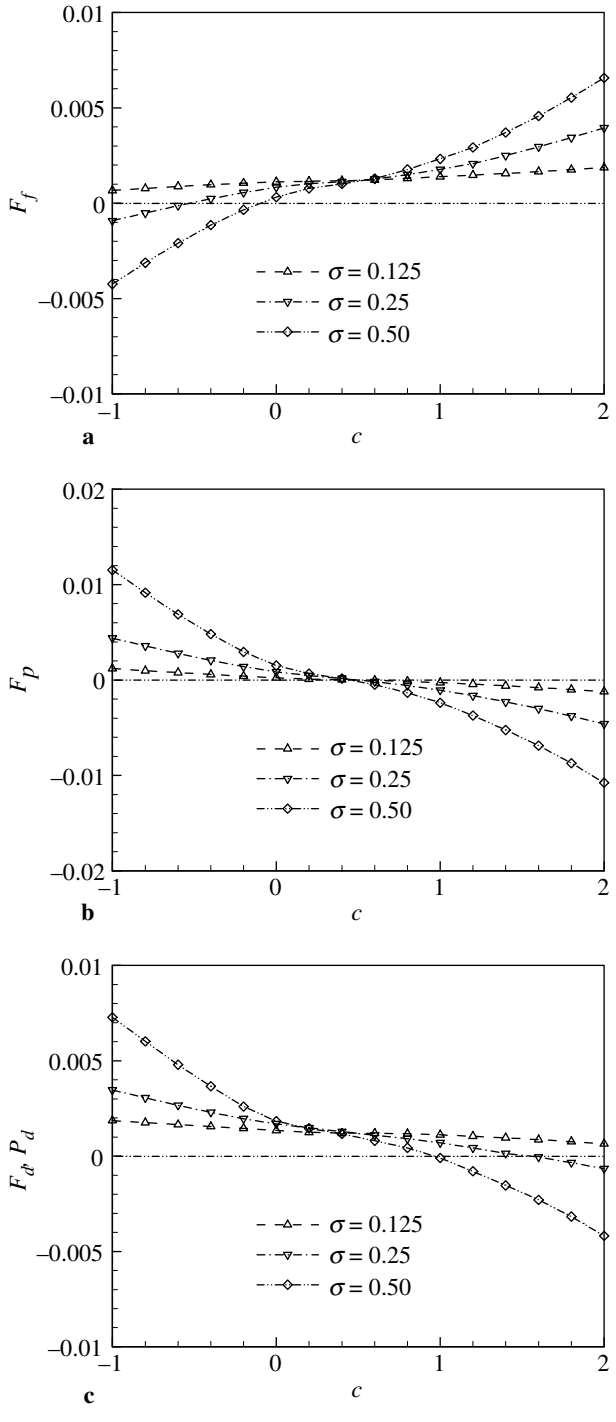

Fig. 10. Variations of the drag force versus C for different σ at $\mathrm{Re} = 2000$: **a** drag force due to the friction force; **b** drag force due to the pressure force; **c** total drag force (or power to overcome the drag force)

The streamline patterns for $\mathrm{Re} = 400$ and 5000 with $\sigma = 0.25$ in the moving frame are shown in Fig. 14. For a stationary wall (i.e., $C = 0$), the separation bubble is formed at $\mathrm{Re} = 2000$ (Fig. 3a) and 5000, however, no separation bubble occurs at $\mathrm{Re} = 400$. In the moving frame, the streamlines exhibit a trapped vortex located over the trough for $\mathrm{Re} = 400$ and 5000 at $C = 0.4$. By comparing with Fig. 4a for $\mathrm{Re} = 2000$, the scale of the trapped

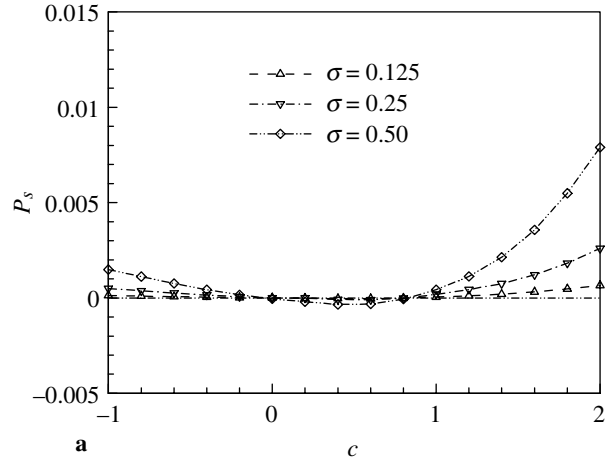

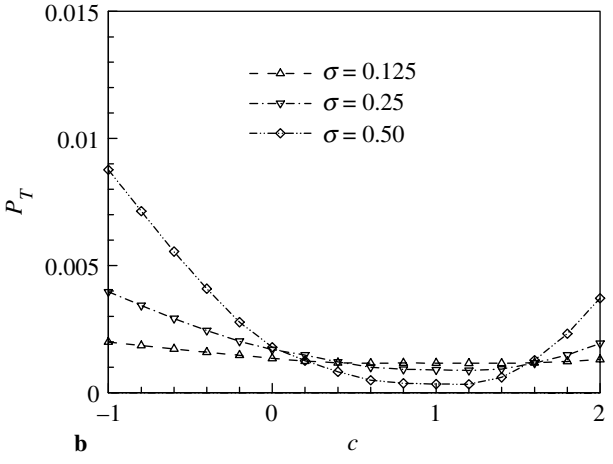

Fig. 11. Variations of the power versus C for different σ at $\mathrm{Re} = 2000$: **a** swimming power; **b** total power

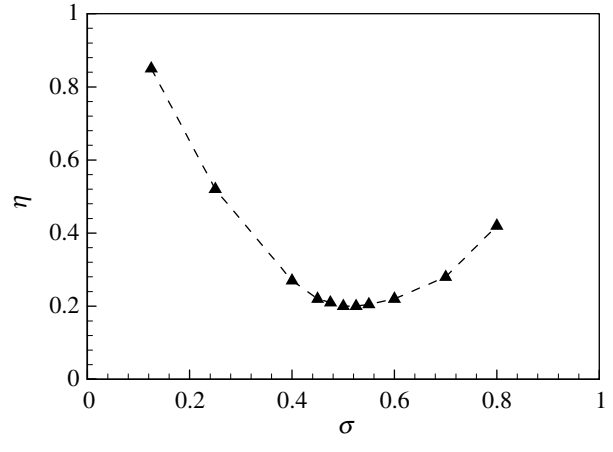

Fig. 12. Total power ratio η versus σ at $C = 1.2$ and $\mathrm{Re} = 2000$

vortex increases reasonably as Re decreases. Further, if $C > 1$, both $-C$ and $1 - C$ are negative. All the streamlines (e.g., for $C = 1.2$ in Fig. 14) point in the opposite x-direction and there is no trapped vortex. Also, when $C < 0$, e.g., $C = -0.4$ in Fig. 14, all the

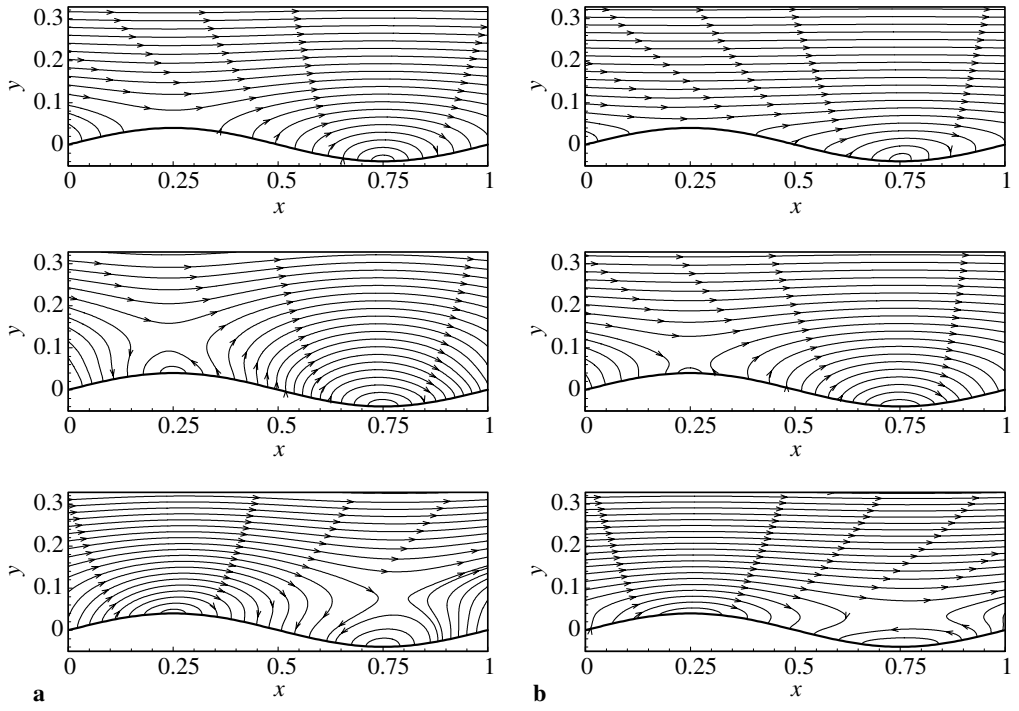

Fig. 13. Streamline pattern in the non-moving frame for different Reynolds numbers at $\sigma = 0.25$: **a** left column with $\mathrm{Re} = 400$, $C = 0.4$, 1.2, and -0.4 from top to bottom; **b** right column with $\mathrm{Re} = 5000$, $C = 0.4$, 1.2, and -0.4 from top to bottom

streamlines point in the x-direction, because both the wall speed $-C$ and the external flow velocity $1 - C$ are positive.

Figure 15 shows the profiles of the friction force F_f, the pressure force F_p and the total drag force $F_d = F_f + F_p$. As C increases, F_f increases and changes from negative to positive value during $-0.8 < C < 0$, but F_p decreases and varies from positive to negative value during $0.2 < C < 0.8$. As shown in Fig. 15c for the total drag force, F_d decreases monotonically with the increase of C, and becomes negative (or thrust force) for $C \geq 1.6$, approximately.

The distributions of P_T and P_s are shown in Fig. 16. As C increases, P_s first decreases smoothly, reaches a minimum for C between 0 and 0.8, and then increases in Fig. 16a. The distributions of P_s coincide closely for those Reynolds numbers during $0 \leq C \leq 0.6$. Then P_s becomes positive for $C \geq 1$. The profiles of the power to overcome the drag force (i.e., P_d) are shown in Fig. 15c. The distributions of the total power P_T versus C for different Re are concave upwards with a minimum around $C = 1.2$ in Fig. 16b. As listed in Table 1, it is reasonable to predict that the total power ratio η is 68% approximately for $\mathrm{Re} = 400$ and 48% for $\mathrm{Re} = 5000$.

4.5 Comparison between the travelling wavy wall and fish swimming

To clarify the wavy motions characterizing steady undulatory swimming in fish, Videler [11] proposed some simple models to analyze the fish-like swimming motions. As an extension of the kinematics analysis, by using computational fluid dynamics to solve the incompressible Navier-Stokes equations, the undulating wave motion, similar to the backbone undulation of

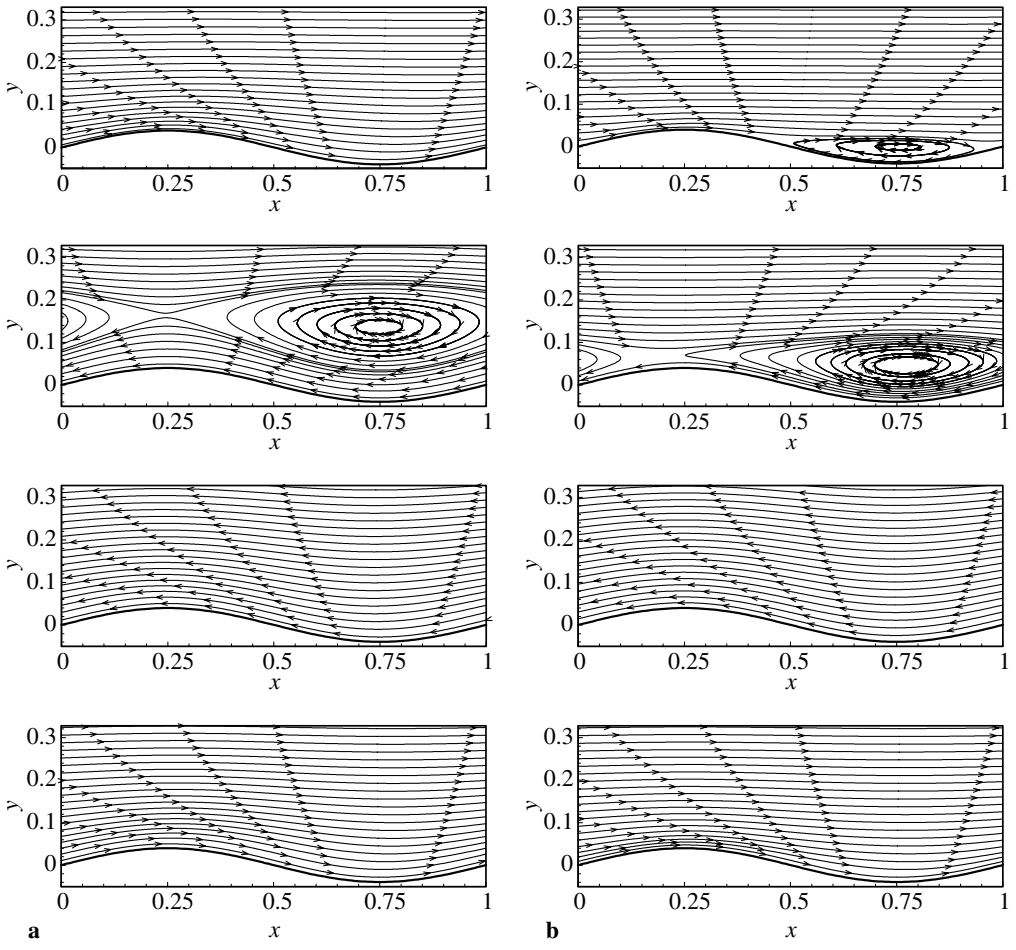

Fig. 14. Streamline pattern in the moving frame for different Reynolds numbers at $\sigma = 0.25$: **a** left column with $\mathrm{Re} = 400$, $C = 0$, 0.4, 1.2, and –0.4 from top to bottom; **b** right column with $\mathrm{Re} = 5000$, $C = 0$, 0.4, 1.2, and -0.4 from top to bottom

swimming fish, is modeled simply as a travelling sinusoidal wave. Based on the results above, it is found that the travelling wavy wall can be optimized to achieve separation suppression, to create thrust, and to minimize net power input.

It is necessary to compare the results of the travelling wavy wall obtained in this study with some typical live fish swimming. Based on measurement of steadily swimming saithe and eel, the movements of saithe and eel were observed as digitized outlines from film frames [38]. The kinematic and morphometric quantities for saithe and eel are listed in Table 2.

The overall flow pattern and dynamics depend strongly on the phase speed C. For upstream travelling wave motion (i.e., $C < 0$), the flow feature is qualitatively similar to that for $C = 0$. The attached shear flow near the travelling wavy wall persists and strengthens with decreasing C, resulting in an increasingly greater drag force and net energy needed for propulsion. For downstream travelling wave motion (i.e., $C > 0$), the flow is significantly altered. As C increases, the separation bubble moves away from the wall, and the separation eddy is weakened and eventually leads to its disappearance at C about 1.0. Based on the understanding of fish-like locomotion, the mean force and power are of primary concern and are analyzed above.

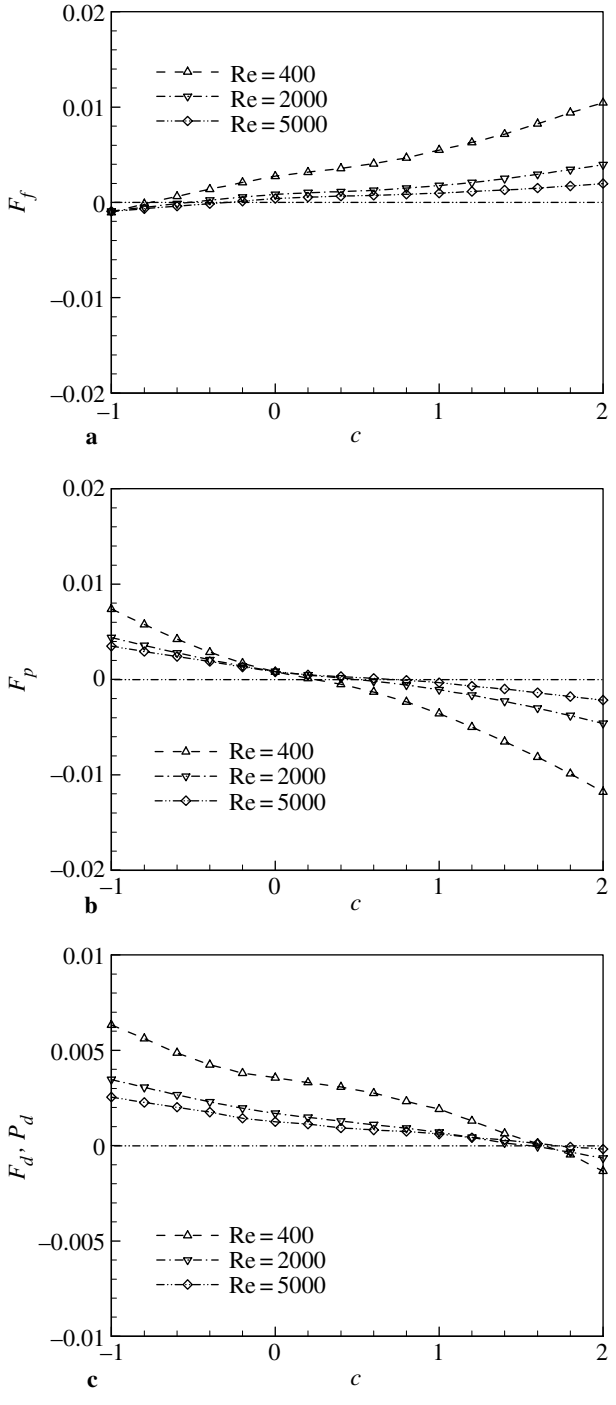

Fig. 15. Variations of the drag force versus C for different Reynolds numbers at $\sigma = 0.25$: **a** drag force due to the friction force; **b** drag force due to the pressure force; **c** total drag force (or power to overcome the drag force)

Of ultimate interest is the net power required for the locomotion, which is the sum of the swimming power and the power required to overcome the total drag. This total power yields a minimum for the net power required at $C = 1.2$, approximately. As listed in Table 2, the ratio of the travelling wave speed and the swimming speed C_S/U_S is 1.21 and 1.26 approximately for steadily swimming saithe and eel. Thus, it is noteworthy that C around 1.2 predicted

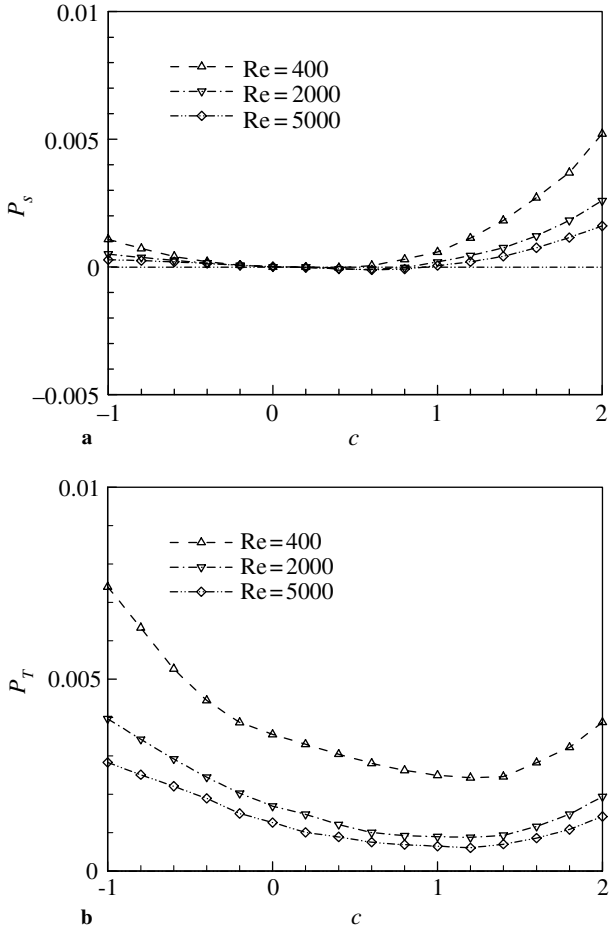

Fig. 16. Variations of the power versus C for different Reynolds numbers at $\sigma = 0.25$: **a** swimming power; **b** total power

Table 2. Kinematic and morphometric quantities for saithe and eel

	Length (L)	Maximum tail amplitude (A/L)	$\sigma_S = 2\pi A/L$	C_S/U_S
Saithe	0.37m	0.083	0.522	1.21
Eel	0.14m	0.102	0.641	1.26

Here, C_S/U_S represents the ratio of the travelling wave speed and the swimming speed.

numerically is the value adopted for travelling wave-like swimming motion of live fish in nature [38], [39].

To explore effective propulsion for the travelling wavy wall, the other important parameter is the amplitude of the travelling wave. Although the wave amplitude used in this study is constant, the results are still reasonable to understand the mechanism of the propulsion for the travelling wavy wall. To clarify the variation of η with σ, as shown in Fig. 12, it is noted that the power ratio η for $0.4 < \sigma < 0.7$ is less than 30%, corresponding to the high propulsive efficiency for a travelling wavy wall. Compared to the data in Table 2 for steadily swimming saithe and eel, the maximum tail amplitudes $\sigma_S = 2\pi A/L \approx 0.522$ and 0.641 are consistent with the present numerical prediction for $0.4 < \sigma < 0.7$.

Acknowledgements

This work was supported by the National Natural Science Foundation of China (Nos. 10332040, 10125210), the Innovation Project of the Chinese Academy of Sciences (Nos. KJCX-SW-L04, KJCX2-SW-L2), and the Programme of Hundred Talent of the Chinese Academy of Sciences.

References

[1] Weis-Fogh, T., Jensen, M.: Biology and physics of locust flight. Proc. Roy. Soc. B. **239,** 415–585 (1956).
[2] Lighthill, M. J.: Aquatic animal propulsion of high hydromechanical efficiency. J. Fluid Mech. **44,** 265–301 (1970).
[3] Lighthill, M. J.: Mathematical biofluiddynamics. Philadelphia: SIAM 1975.
[4] Maxworthy, T.: The fluid dynamics of insect flight. Ann. Rev. Fluid Mech. **13,** 329–354 (1981).
[5] Wu. T. Y.: On theoretical modeling of aquatic and aerial animal locomotion. Adv. Appl. Mech. **38,** 291–353 (2001).
[6] Phlips, P. J., East, R. A., Pratt, N. H.: An unsteady lifting line theory of flapping wings with application to the forward flight of birds. J. Fluid Mech. **112,** 97–125 (1981).
[7] Triantafyllou, M. S., Triantafyllou, G. S., Gopalkrishnan, R.: Wake mechanics for thrust generation in oscillation foils. Phys. Fluids **3,** 12–26 (1991).
[8] Smith, M. J. C., Wilkin, P. J., Williams, M. H.: The advances of an unsteady method in modeling the aerodynamic forces on rigid flapping wings. J. Exp. Biol. **199,** 1073–1083 (1996).
[9] Anderson, J. M., Streitlien, K., Barrett, D. S., Triantafyllou, M. S.: Oscillating foils of high propulsive efficiency. J. Fluid Mech. **360,** 41–72 (1998).
[10] Birch, J. M., Dickinson, M. H.: The influence of wing–wake interactions on the production of aerodynamic forces in flapping flight. J. Exp. Biol. **206,** 2257–2272 (2003).
[11] Videler, J. J.: Swimming movements, body structure and propulsion in cod Gadus morhua. In: Vertebrate locomotion (Day, M. H., ed.), pp. 1–27. London: Academic Press 1981.
[12] Gray, J.: Studies in animal locomotion: I. The movement of fish with special reference to the eel. J. Exp. Biol. **10,** 88–104 (1933).
[13] Carling, J., Williams, T.L., Bowtell, G.: Self-propelled anguilliform swimming: simultaneous solution of the two-dimensional Navier-Stokes equations and Newton's laws of motion. J. Exp. Biol. **201,** 3143–3166 (1998).
[14] Anderson, E. J., McGillis, W. R., Grosenbaugh, M. A.: The boundary layer of swimming fish. J. Exp. Biol. **204,** 81–102 (2001).
[15] Liao, J. C., Beal, D. N., Lauder, G. V., Triantafyllou, M. S.: The Karman gait: novel body kinematics of rainbow trout swimming in a vortex sheet. J. Exp. Biol. **206,** 1059–1073 (2003).
[16] Gray, J.: Studies in animal locomotion. J. Exp. Biol. **13,** 192–199 (1936).
[17] Wu. T. Y.: Swimming of a waving plate. J. Fluid Mech. **10,** 321–344 (1961).
[18] Wu, T. Y.: Hydromechanics of swimming propulsion. Part 1. Swimming of a two-dimensional flexible plate at variable forward speeds in an inviscid fluid. J. Fluid Mech. **46,** 337–355 (1971).
[19] Cheng, J. Y., Zhuang, L. X., Tong, B. G.: Analysis of swimming 3-D waving plate. J. Fluid Mech. **232,** 341–355 (1991).
[20] Abrams, J., Hanratty, T. J.: Relaxation effects observed for turbulent flow over a wavy surface. J. Fluid Mech. **151,** 443–455 (1985).
[21] Harper, D. G., Blake, R. W.: Fast-start performance of rainbow trout (Salmo gairdneri) and Northern Pike (Esox Lucius). J. Exp. Biol. **150,** 321–342 (1990).
[22] Barrett, D. S., Triantafyllou, M. S., Yue, D. K. P., Grosenbaugh, M. A., Wolfgang, M. J.: Drag reduction in fish-like locomotion. J. Fluid Mech. **392,** 183–212 (1999).
[23] Triantafyllou, M. S., Triantafyllou, G. S., Yue, D. K. P.: Hydrodynamics of fishlike swimming. Ann. Rev. Fluid. Mech. **32,** 33–53 (2000).
[24] Shen, L., Zhang, X., Yue, D. K. P., Triantafyllou, M. S.: Turbulent flow over a flexible wall undergoing a streamwise travelling wave motion. J. Fluid Mech. **484,** 197–221 (2003).

[25] Tokumaru, P. T., Dimotakis, P. E.: Rotary oscillation control of a cylinder wake. J. Fluid Mech. **224,** 77–90 (1991).
[26] Lu, X. Y., Sato J.: A numerical study of flow past a rotationally oscillating circular cylinder. J. Fluids Structs. **10,** 829–849 (1996).
[27] Lu, X. Y.: Numerical study of the flow behind a rotary oscillating circular cylinder. Int. J. Comp. Fluid Dyn. **16,** 65–82 (2002).
[28] Taneda, S., Tomonari, Y.: An experiment on the flow around a waving plate. J. Phys. Soc. Japan **36,** 1683–1689 (1974).
[29] Kendall, J. M.: The turbulent boundary layer over a wall with progressive surface waves. J. Fluid Mech. **41,** 259–281 (1970).
[30] De Angelis, V., Lombardi, P., Banerjee, S.: Direct numerical simulation of turbulent flow over a wavy wall. Phys. Fluids **9,** 2429–2442 (1997).
[31] Calhoun, R. J., Street, R. L.: Turbulent flow over a wavy surface: neutral case. J. Geophys. Res. **106,** 9277–9293 (2001).
[32] Zang, Y., Street, R. L., Koseff, J. R.: A non-staggered grid, fractional step method for time-dependent incompressible Navier-Stokes equations in curvilinear coordinates. J. Comp. Phys. **114,** 18–33 (1994).
[33] Perng, C. -Y., Street, R. L.: Three-dimensional unsteady flow simulations: alternative strategies for a volume-averaged calculation. Int. J. Numer. Meth. Fluids **9,** 341–362 (1989).
[34] Lu, X. Y.: A study of oscillating flows over propagating ripples: Part I. Steady streaming. J. Hydrodyn., Ser. B, **11**, 15–22 (1999).
[35] Lu, X. Y.: A study of oscillating flows over propagating ripples: Part II. Vorticity dynamics. J. Hydrodyn., Ser. B, **12**, 8–15 (2000).
[36] Hsu, C. T., Lu, X. Y., Kwan, M.K.: LES and RANS studies of oscillating flows over a flat plate. ASCE J. Engng Mech. **126,** 186–193 (2000).
[37] Batchelor, G. K.: An introduction to fluid dynamics. Cambridge: Cambridge Press 1970.
[38] Videler, J. J.: Fish swimming. London: Chapman & Hall 1993.
[39] Videler, J. J., Hess, F.: Fast continuous swimming of two pelagic predators, saithe (pollachius virens) and mackerel (scomber scombrus): a kinematic analysis. J. Exp. Biol. **109,** 209–228 (1984).
[40] Li, X. M., Lu, X. Y., Yin, X. Z.: Visualization on fish's wake. Proc. SPIE **4537,** 473–476 (2002).

Authors' address: X.-Y. Lu and X.-Z. Yin, Department of Modern Mechanics, University of Science and Technology of China, Hefei, Anhui 230026, P.R. China (E-mail: xlu@ustc.edu.cn)